Electrochimica Acta 378 (2021) 138112

Contents lists available at ScienceDirect

Electrochimica Acta

journal homepage: www.elsevier.com/locate/electacta

Resistivity of mesopore-confined ionic liquid determined by electrochemical impedance spectroscopy

Gibson P. Scisco[a,*], Mark E. Orazem[b], Kirk J. Ziegler[b], Kevin S. Jones[a]

[a] Department of Materials Science and Engineering, University of Florida, 549 Gale Lemerand Drive, PO BOX 116400, Gainesville, FL 32611, USA
[b] Department of Chemical Engineering, University of Florida, Gainesville, FL 32611, USA

ARTICLE INFO

Article history:
Received 23 December 2020
Revised 5 March 2021
Accepted 6 March 2021
Available online 15 March 2021

Keywords:
Carbon nanotubes
Supercapacitor
Ionic liquid
Anodized aluminum oxide
Electrochemical double layer capacitor

ABSTRACT

Ordered carbon nanotube (CNT) arrays with pore diameter 24.4 ± 4.6 nm formed within anodized aluminum oxide (AAO) bonded to Si were used as electrodes for supercapacitors with neat EMIM-BF4 ionic liquid as the electrolyte. A series of devices with increasing AAO thickness (equal to CNT length) were tested using electrochemical impedance spectroscopy (EIS). Data were fit using the de Levie model of porous electrodes to determine the electrochemically active surface area and the in-pore electrolyte resistivity. The results indicate that uncatalyzed chemical vapor deposition (CVD) of CNTs in AAO can lead to blocked CNTs and reduced active area. The average resistivity of the electrolyte within the pores across the four devices tested was determined to be approximately 383 Ω cm, more than five times higher than the reported bulk resistivity of 70.9 Ω cm. It is possible that the enhanced resistivity is due to hydrophilic surface functionalities on the surface of the CNTs.

1. Introduction

Due to the ever-increasing demand for highly cyclable electrochemical energy storage, electrochemical double layer capacitors (EDLCs), sometimes called supercapacitors, have attracted much research interest in the last decade [1–3]. Supercapacitors have lower energy density than Li-ion batteries owing to their surface-sensitive charge storage mechanism. The energy density of an EDLC is expressed by

$$E = \frac{1}{2}CV^2 \tag{1}$$

where V is the voltage across the capacitor and the capacitance is given as

$$C = \frac{\in A}{d} \tag{2}$$

where ϵ is the permittivity of the medium separating the electrodes, A is the electrode area, and d is the charge separation distance. To maximize EDLC energy, large area electrodes with small ion separation capable of high voltage operation are required.

The electrode area can be increased by using porous electrodes. When the pores of the electrode are size-matched to the diameter of electrolyte ions, the ion-electrode separation distance can be reduced and capacitance increased [4,5]. The voltage on the device is limited by the electrolyte, with aqueous electrolytes restricted to $<$ 1.23 V due to the hydrolysis of water at this potential. A family of organic salt electrolytes called ionic liquids are of interest for EDLC applications due to their high electrochemical stability windows of 3 – 6 V [6]. Therefore, rational design of EDLCs focuses on creating high surface area porous electrodes with large numbers of ultramicropores ($<$ 2 nm) and with solvent free ionic liquids as electrolytes. Networks of all-micropore systems will exhibit high resistance due to high tortuosity, which will inhibit the attractive high-power capabilities of supercapacitors [7,8]. Therefore, ultramicropores are connected by mesopore networks which are thought to keep the resistivity of the system relatively low by reducing tortuosity as compared to an all-micropore system [9]. However, there is evidence that even in mesopores where steric transport restrictions are unexpected [10], solvent-free ionic liquids can experience greatly increased resistivity as compared to the bulk values.

Previous work has demonstrated increased ionic liquid resistivity in mesopores using measurements of single pores in track-etched PET and disordered pore clusters in anodized Si [11,12]. These measurements showed that the resistivity of ionic liquids in mesopores was increased by several times the bulk value, but the tested structures are very different from functional EDLC electrodes. Our group recently demonstrated a novel method of creating on-chip EDLCs by bonding thick anodized aluminum oxide (AAO) templates to Si wafers [13]. AAO is a widely used nanotemplate composed of ordered, monodisperse pores aligned normal to

* Corresponding author.
E-mail address: gpscisco@ufl.edu (G.P. Scisco).

https://doi.org/10.1016/j.electacta.2021.138112
0013-4686/

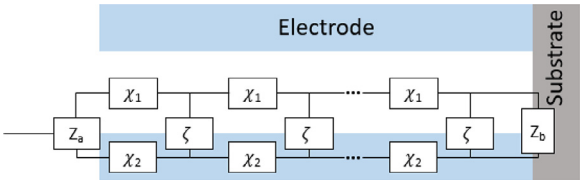

Fig. 1. A schematic showing a single pore of a porous electrode and its associated impedances. In the de Levie model, χ_1 is modeled as a resistor and ζ is modeled as a CPE. All other impedances are set to 0. An additional ohmic resistance R_e can be added to account for the effects of the electrode separator and apparatus resistances.

the aluminum face, and vertically-aligned CNT (VACNT) electrodes can be made by depositing CNTs into the pores of the AAO. The highly controllable pore structure of these electrodes allows for detailed analysis of their electrochemical impedance spectroscopy (EIS) response [14,15].

EIS is a widely used method of characterizing electrochemical systems in which a probing ac potential of small magnitude (generally ~10 mV) interacts with a system of interest to generate an ac current. The complex impedance is determined from the ratio of the potential and current phasors. EIS analysis of porous electrodes has been historically accomplished through the transmission line model. De Levie's formulation of the transmission line [16] contains parameters of electrolyte resistivity, but this value cannot be extracted from the model without the precise pore dimensions of the electrode. Recently, de Levie-based EIS models of polymer electrolyte fuel cells were used to calculate the ionic conductivity within the membrane using mercury porosimetry to determine the pore size distribution [17].

In the present work, pouch cell EDLCs were made from VACNT electrodes with neat ionic liquid electrolyte (1-ethyl-3-methylimidazolium tetrafluoroborate, EMIM-BF4, Iolitec, 99%). By controlling the anodization and CVD parameters, the pore structure (pore diameter, length, and density) can be easily determined through electron microscopy. EIS spectra were fit using de Levie's model with an interfacial pore impedance modeled by a CPE. Specific capacitance was calculated using Brug's formula, and the electrolyte resistivity within the pores was calculated based on the equations of de Levie.

2. Theory

The most general transmission line is shown in Fig. 1 and includes 5 impedance terms to model the electrode [18]. The impedance at the interface of the porous layer and the bulk electrolyte is given as Z_a and that of the pore bottom is Z_b. The Z_a and Z_b terms are only significant when the electrode area outside of the pores is relatively large compared to the in-pore area [19], or when the pore bottom has a significant impedance [20]. The impedance through the electrolyte within the pores is given as χ_1, and its behavior can be modelled as a resistor. The confined electrolyte within pores is known to behave quite differently compared to the bulk response [21–23]. The impedance within the electrode material pore walls is labeled χ_2 and is also generally considered as a resistor. More complex representations of χ_2 have been used in semiconducting systems such as TiO_2 nanotubes [20]. The impedance within the pore at the electrode-electrolyte interface, i.e. the impedance of the pore walls, is given as ζ and takes the form of a capacitance.

The de Levie model is a particular case of the porous electrode, originally published in 1964[16]. The model assumes: (1) pores are cylindrical with only the pore walls conducting, (2) the electrode is ideally polarizable, (3) the pore is filled with electrolyte of constant resistivity, and (4) the potential gradient is only along the pore axis with no radial dependence. This model is equivalent to setting Z_a, Z_b, and χ_2 equal to 0, and modeling χ_1 as a resistor and ζ as a capacitor or constant phase element (CPE). The closed form is given in Eqs. (3) and (4), following the derivation of Lasia [24] as

$$Z = R_e + \frac{R_\Omega}{\sqrt{\beta}} \coth\left(\sqrt{\beta}\right) \tag{3}$$

with

$$\beta = 2n\pi rLR_\Omega \zeta^{-1} \tag{4}$$

where R_e is the ohmic resistance, R_Ω is the total resistance of the electrolyte within the pores, n is the total number of pores, r is the average pore radius, and L is the average pore length. R_Ω can be used via

$$R_\Omega = \frac{\rho_e L}{n\pi r^2} \tag{5}$$

to determine the resistivity of the electrolyte within the pores, ρ_e.

If the interfacial impedance is modeled with an ideal capacitance as

$$\zeta = (j\omega C)^{-1} \tag{6}$$

then the Nyquist plot based on Eqs. (3) and (4) will display a 45° line at high frequencies and a vertical line below ω_{bp}, the breakpoint frequency, as in Figs. 8.3 and 9.3 from Lasia [24]. Generally, physical systems behave non-ideally, with phase angles less than 45° in the high frequency region and less than 90° in the low frequency region. This non-ideality can be taken into account by replacing ζ in Eq. (4) with a CPE, i.e.

$$\zeta = \left[(j\omega)^\alpha Q\right]^{-1} \tag{7}$$

where Q and α are the CPE coefficients.

Simulations of the de Levie model with interfacial capacitance as a CPE were performed and are given in Fig. 2. Increasing R_e in Fig. 2a simply shifts the spectrum to higher Z_r; R_e does not affect the shape of the plot. In Fig. 2b, increasing R_Ω increases the length of the high frequency arm and pushes the breakpoint frequency to lower values for a given pore radius and length. The values of both R_e and R_Ω can be read directly from the Nyquist plot as depicted in Fig. 2a,b. The effect of Q on impedance is shown in Figure 2c. A higher Q results in lower |Z|, but it does not change the shape of the spectrum. A higher value of Q generally results in a higher effective capacitance based on the Brug formula (Eq. (9)), depending on α and the system resistances. The dispersion coefficient α determines the angle of the two branches of the Nyquist plot as seen in Fig. 2d. The effect is more noticeable at frequencies lower than ω_{bp}, but smaller values of α will also result in a high frequency arm lower than 45° in the Nyquist plot.

The impedance of the electrolyte within the pore reduces the penetration depth of the applied ac voltage according to the signal frequency. At high frequencies, the penetration depth is low and only a small amount of the pore wall is being charged. Only at low frequencies can the entire pore "feel" the ac signal. This dependence of the penetration depth on frequency results in a breakpoint frequency, ω_{bp}, where in the Nyquist plot the impedance angle switches from shallow to more vertical with the exact angle dependent on α. This breakpoint frequency is determined by the dimensions of the pores and the resistivity of the electrolyte [19] and is given as

$$\omega_{bp} = \frac{9r}{4\rho_e L^2 C_{sp}} \tag{8}$$

where C_{sp} is the specific capacitance in F cm^{-2} based on the total porous electrode area.

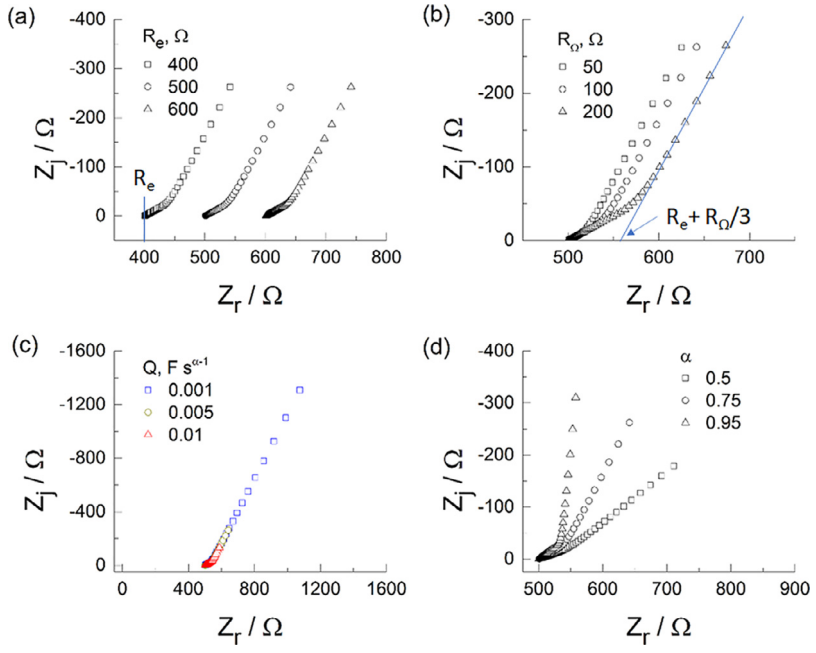

Fig. 2. Simulated Nyquist plots of the de Levie formula showing the effect of increasing a) R_e (pushing plot to the right, no change in shape), b) R_Ω (increasing length of high frequency 45° arm), c) Q (decreasing magnitude of impedance |Z|), and d) α (changing slope of both high and low frequency regions). In each series unless otherwise noted, parameters were held constant at R_e = 500 Ω, R_Ω = 100 Ω, Q = 0.005 F $s^{\alpha-1}$, and α = 0.75.

When interfacial impedance ζ is modeled by a CPE, Q is in units of F $s^{\alpha-1}$ and is not a direct measurement of capacitance. The Brug formula [25]

$$C_{sp} = Q^{\frac{1}{\alpha}}\left(R_e + \frac{R_\Omega}{3}\right)^{\frac{1-\alpha}{\alpha}} \tag{9}$$

can be used to calculate the effective capacitance based on the CPE parameters and the system resistances. The combination of the de Levie model and the Brug formula has been used extensively by Lasia et al. to characterize the impedance and capacitance of porous metal electrodes [19,26–28]. The transmission line model has been previously applied to anodized TiO_2 nanotubes, structurally similar to AAO, and values of the TiO_2 resistance and barrier oxide thickness were extracted [20]. The de Levie model has previously been applied to AAO based systems in the form of electroless Au-plated AAO, however, the analysis was limited, only extracting the total electrode resistance from the high frequency impedance [29]. Obermaier et al. used similar EIS techniques together with pore size distributions of PEMFC membranes to determine ionic conductivity within the membranes [17].

3. Experimental

A detailed description of the VACNT electrode fabrication process has been published elsewhere [13]. Briefly, high purity Al sheeting (99.999%, Goodfellow) was doubly anodized in 0.3 M oxalic acid at 40 V and 15°C. At the end of the second anodization, the voltage was linearly decreased by 1 V s^{-1} to 0 V to remove the barrier oxide layer at the base of the AAO pores. The anodized Al films were then bonded to Si wafers and CNTs were deposited *in situ* with the bonding process. The resulting CNTs have inner diameters of 24.4 ± 4.6 nm, an areal density of 9.9 × 10^9 cm^{-2}, and a length controlled to within 1.4 μm by the anodization time. The pore structure of these samples was determined through SEM (FEI Nova 430 FESEM) and TEM (FEI Tecnai F20 S/TEM).

Symmetrical pouch cell supercapacitors were made using two VACNT electrodes separated by glass fiber filter paper (0.7 μm pore size, 0.46 mm thick, MilliporeSigma) sealed in a Mylar pouch. The electrodes and separators were dried overnight in a vacuum oven before being transferred to an Ar glovebox with a moisture probe reading < 2 ppm H_2O. Inside the glovebox, the separator was wetted with 0.5 mL of neat 1-ethyl-3-methylimidazolium tetrafluoroborate (EMIM-BF4, ≥99%, Iolitec) as the electrolyte.

As a control sample, the same Al discs as used for anodization were polished on SiC polishing paper to a final grit of P4000. The polished Al discs were then coated with evaporated carbon to mimic the CVD grown CNTs. The evaporated carbon layer was 104 nm thick determined by stylus profilometry. The roughness factor of the control sample was determined by AFM (SPM/AFM Dimension 3100) to determine a precise control surface area.

EIS was performed using a VersaSTAT 3 potentiostat (Princeton Applied Research). Testing was performed at open circuit potential with an amplitude of 10 mV on the frequency range 10^5 – 10^{-1} Hz. Visual inspection of the EIS data from several VACNT electrodes was used to determine the applicability of the de Levie model, and only those samples which could reasonably be expected to be fit by the model were used to determine in-pore electrolyte resistivity. EIS data was analyzed using non-linear least squares fitting in the measurement model software, which was also used to check the Kramers-Kronig consistency [30]. Error bars for resistivity calculations were determined through Monte Carlo simulations with 10,000 iterations, assuming a normal distribution of each variable using the calculated average and standard deviation.

4. Results and discussion

The surface of the non-porous control sample imaged through AFM is given in Fig. 3a. The sample was not perfectly smooth, with an average roughness of 149 nm. This resulted in a roughness factor of 1.12. The top-down view of the CNTs deposited within the pores of the AAO from SEM is shown in Fig. 3b. These images were used to determine the CNT pore diameter as 24.4 ± 4.6 nm (n = 114).

The EIS spectrum of the control sample is given in Fig. 4. Since this sample was not porous, it was fit with an R-CPE series circuit rather than the de Levie model. The fit to this simple model is

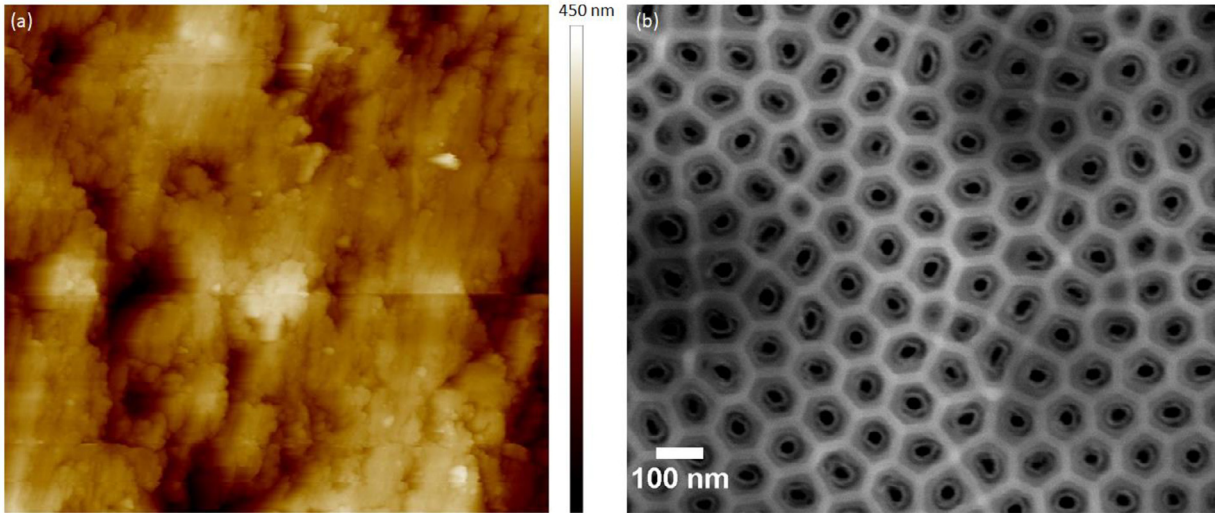

Fig. 3. Surface of (a) carbon coated polished Al control using atomic force microscopy. The roughness factor of the polished sample was determined to be 1.12 after carbon deposition. (b) CNT-filled AAO imaged through SEM. The pore diameter was determined to be 24.4 ± 4.6 nm and pore density was 9.9 × 10^9 cm^{-2}.

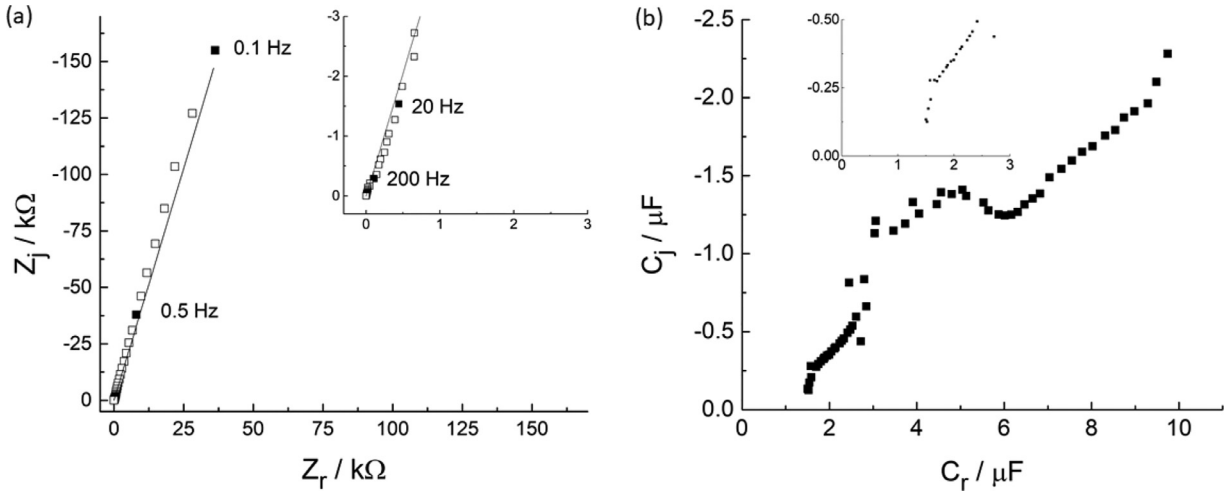

Fig. 4. The carbon coated Al disc control sample was analyzed through R-CPE fitting of the EIS and Cole-Cole representation of the complex capacitance. EIS spectrum of the carbon coated Al control sample (a), with measured data in unfilled squares and the fit to the R-CPE model as a black line. Based on the fitting, Q = 9.8 μF $s^{\alpha-1}$, α = 0.848, and R_e = 1.76 Ω. The Cole-Cole representation of the same sample (b), with inset showing high-frequency region and asymptote approaching 1.52 μF.

good, although there is some lack of fit in the high frequency region. The ohmic resistance was determined to be 1.75 ± 0.06 Ω, Q was 9.80 ± 0.12 μF $s^{\alpha-1}$, and α was 0.848 ± 0.002. Using the Brug formula (Eq. (9)), these CPE values result in a capacitance of 1.38 μF. The capacitance was verified using the measurement model approach which has previously been used to determine the capacitance of flat oxide films exhibiting CPE behavior [31]. Using the measurement model, the capacitance was determined to be 1.49 ± 0.08 μF. The Cole-Cole representation of the complex capacitance is given in Fig. 4b, and the high frequency asymptote associated with double layer capacitance approaches 1.52 μF. These three values are in very good agreement with one another and offer three independent calculations of the control sample's capacitance from the EIS data. For determination of the active area of the VACNT samples, the Q value determined from EIS of 9.8 μF $s^{\alpha-1}$ was used.

The measured EIS spectra and the de Levie fitting for each sample are shown in Fig. 5. The low values of R_e for all samples indicates that the *in situ* barrier layer thinning was successful independent of template thicknesses. For the thinnest sample in Fig. 5a, there is some unexpected behavior at high frequency. Instead of a straight line at ~45°, there appears to be part of a depressed semicircle. This may be due to the impedance of the electrode outside the pores [19]. For this sample, the pore area was calculated based on geometry of the pores to be 390 cm^2, and the area of the tips of the CNTs to be 0.338 cm^2, a ratio of 1153:1. Attempts to fit this data taking into account the capacitance of the electrode outside the pores resulted in a worse fit than the de Levie model. All other samples show good fitting in low and high frequency by the de Levie model. The confidence intervals for the fitted values were calculated to be < ± 6%, even for the 18 μm sample. From Fig. 5, the value of |Z| decreases as the template thickness increases, while the angle of the low frequency arm remains relatively constant. The decrease in |Z| is associated with an increase in Q for a constant value of α.

Based on the data presented in Fig. 5, the interfacial impedance is well-fit by a model that invokes a CPE. Brug et al. [25] initially proposed that CPE behavior originated from surface roughness. However, Alexander et al. [32] showed that, for moderate roughness factors, the frequency dispersion associated with surface roughness is seen at higher frequencies than those analyzed in the present work. CPE behavior in porous electrodes has previously been attributed to time constant distribution arising from

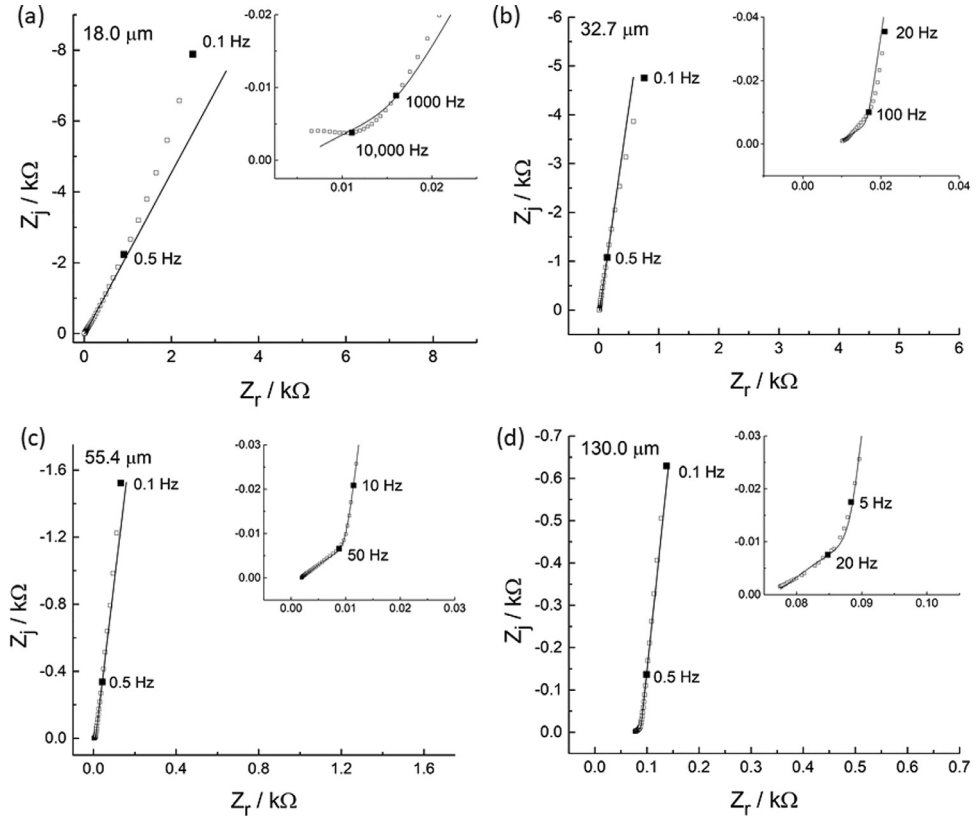

Fig. 5. EIS spectra of VACNT electrodes of AAO thickness (a) 18 μm, (b) 32.7 μm, (c) 55.4 μm, and (d) 130 μm. The measured data in each plot is shown as unfilled squares, and the fit to the de Levie model as a black line. The scale shows a decrease in |Z| as AAO thickness increases, indicating increased Q as expected for larger surface area. The shape is similar, indicating similar α values except in the thinnest case. R_e can be estimated based on the high frequency limit of the Nyquist plot, and $R_e + R_\Omega/3$ can be estimated by linear extrapolation of the low frequency region to $Z_j = 0$

Table 1
CPE parameters Q and α taken from fitting EIS data. The ratio of the control Q to that of the porous electrodes was used to determine the electrochemically active surface area of the electrodes. The expected area is based on the measured pore diameter, length, and density from SEM. Confidence intervals are given as 1 σ.

AAO Thickness / μm	α	Q / μF $s^{\alpha-1}$	Q ratio	Q-derived Area / cm^2	Expected Area / cm^2
Control	0.848 ± 0.002	9.80 ± 0.12	1.00	5.68	5.68
18.0	0.737 ± 0.004	174 ± 15	17.77	101	390
32.7	0.925 ± 0.002	320 ± 12	32.65	185	707
55.4	0.939 ± 0.001	1010 ± 1	102.86	584	1197
130.4	0.946 ± 0.001	2460 ± 5.5	251.37	1428	2821

different charging times for pores of different size [33–35]. The model used in the present work treats the CPE as a property of the pore wall surface. This analysis is consistent with the observation of CPE behavior for the disk geometry. The work of Alexander et al. [36] suggests that the local CPE cannot be attributed to local variations in capacitance. Other explanations for CPE behavior such as the coupling of charging and faradaic current [37] and anomalous diffusion [38] have been suggested, but these seem inappropriate for the present system. Thus, while the experimental data exhibits CPE behavior, the emphasis of the present work is on the electrolyte resistivity within the pores. Future work may be directed at providing a physical explanation of the observed CPE behavior which is consistent with the assumptions of the de Levie model.

The values of Q and α for each sample are shown in Table 1. The electrochemically active surface area of the VACNT electrodes was determined by calculating the ratio of $Q_{control}$ to that of the porous sample and multiplying this ratio by the surface area of the control sample determined by AFM. The electrochemically active area was much lower than the expected area calculated based on the measured dimensions of the pores. The ratio of the electrochemically determined area and the geometrically determined area increased as template thickness increased. This ratio was 0.259 and 0.262 for the 18 and 32.7 μm samples, respectively, and 0.488 and 0.506 for the 55.4 and 130 μm thick samples, respectively. The increase in the active-to-expected area ratio indicates that the reduced area is dependent on pore length.

The visually determined ω_{bp} values as well as resistance values R_e and R_Ω determined by data fitting are given in Table 2. R_e varies somewhat sample to sample and is affected by device construction, but it is unrelated to the electrolyte behavior within the pores. R_Ω is directly proportional to pore length, and inversely proportional to pore number and pore cross section, see Eq. (5). Since pore number and radius are assumed to be constant between devices, and ρ_e is also assumed to be constant between devices of the same pore radius, then R_Ω should increase with increasing pore length (AAO thickness). This relationship holds except for the thinnest sample of 18 μm, where R_Ω is anomalously high. Based on R_Ω from the three thicker samples, the value of R_Ω for the 18 μm thick sample would be expected to be ~1 Ω. The ω_{bp} values

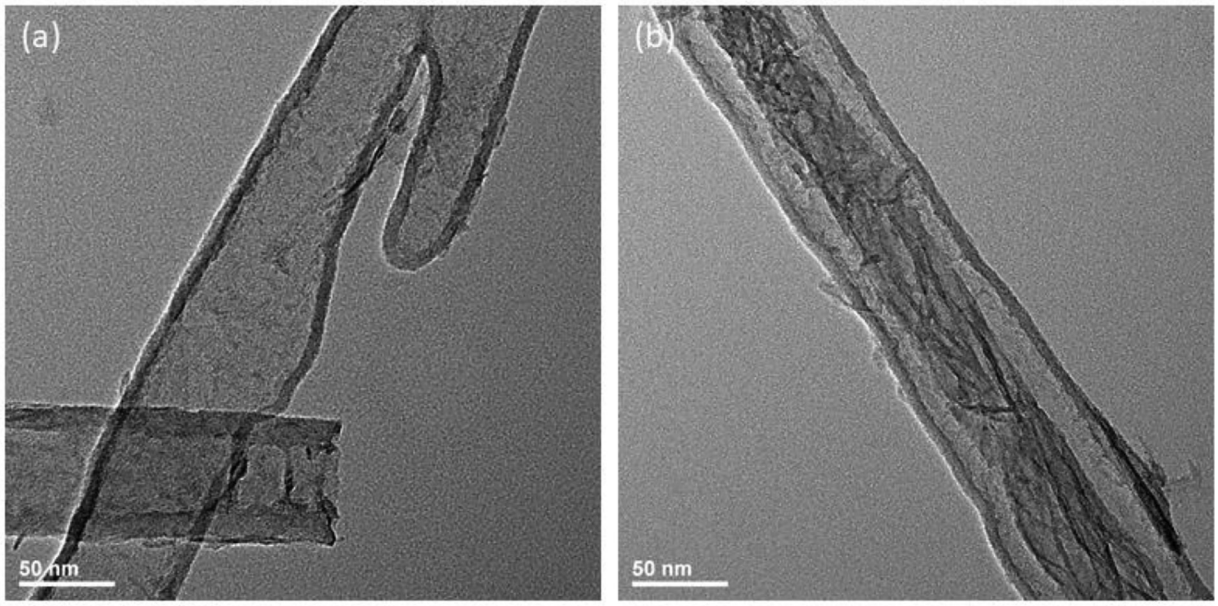

Fig. 6. High resolution bright-field TEM of individual CNTs freed from the AAO template by washing in 5 M NaOH. Most tubes are clear of blockages as in (a), but some tubes as in (b) do show signs of possible blockages either as complete tube filling or dendrite-type growths across the tube interior.

Table 2
Fitted values of R_e and R_Ω with visually estimated ω_{bp} from Nyquist plots. Since the breakpoint frequency is estimated based on the Nyquist plot, no confidence interval is given. To determine error bars of the electrolyte resistivity calculated from ω_{bp}, an error of 10% was assigned to this variable in the Monte Carlo simulations.

AAO Thickness / μm	R_e / Ω	R_Ω / Ω	ω_{bp} / rad s^{-1}
18.0	4.63 ± 0.225	28.27 ± 1.72	7904
32.7	8.89 ± 0.077	21.41 ± 0.59	499.1
55.4	1.75 ± 0.007	23.44 ± 0.15	250.1
130.4	76.43 ± 0.082	33.61 ± 0.53	62.83

Table 3
Specific capacitance values of each electrode calculated using the Brug formula to convert CPE parameters to specific capacitance.

AAO Thickness / μm	C_{sp} / μF cm^{-2}
Control	0.24 ± 0.02
18	0.21 ± 0.03
32.7	1.13 ± 0.08
55.4	1.28 ± 0.05
130	1.58 ± 0.08

should be inversely proportional to the square of the pore length, and this frequency does decrease as template thickness increases as expected.

Individual CNTs were imaged via TEM by etching an AAO template of ~30 μm thickness completely in NaOH and capturing the freed CNTs. In Fig. 6a, some tubes form what look like blockages or bridges [39]. In Fig. 6b, one tube appears almost completely filled with carbonaceous material. EIS data indicated that 50 – 75% of the expected area was electrochemically inactive. The TEM images in Fig. 6 suggest that the area difference between the electrochemically active and expected area could be due to blocked pores. Counting blockages in the TEM images, only ~15% of the imaged CNTs were blocked. However, the sample size in TEM is extremely low and may not provide an accurate measure of the pore blockages. Furthermore, most blockages were seen at the tips of CNTs, which may indicate that the tubes are more likely to snap during sample preparation at the blockage points and could be underrepresented in TEM.

Between the reduced electrochemically active area and the tube blockages imaged via TEM, the data indicates that the carbon growth during CVD does not occur simultaneously along the entire pore structure. Instead, dendritic-type growth is seen at specific points on the AAO pore wall. These dendrites can lead to blockages within the CNTs. Other blockages may be caused by complete filling of CNTs with carbonaceous material. The electrochemical results indicate that the CNT blockages are more prevalent in thinner AAO samples, indicating that the CVD reaction rate proceeds more quickly in AAO with lower total area. During the anodization process, pores can branch off as the pore morphology evolves to its self-ordered state. These branches might result in some pores which initiate on the surface but do not traverse the entire AAO film, instead being pinched off by neighboring pores. However, for thicker templates there is more opportunity for pores to branch during anodization, yet the area ratio improves as template thickness increases. Therefore, the branching process is not thought to explain the observed decrease in electrochemical surface area.

The specific capacitance, C_{sp}, of the VACNT electrodes was calculated based on the Brug formula, Eq. (9), and the results are given in Table 3. For a given electrode/electrolyte system, the specific capacitance should be constant, however, C_{sp} is seen to be approximately an order of magnitude lower in the 18 μm sample compared to the other CAAS electrodes. Also, the planar control sample showed a specific capacitance of only 0.24 μF cm^{-2}, two orders of magnitude lower than the often used benchmark value of 20 μF cm^{-2} for a metallic electrode in a dilute aqueous electrolyte [40]. It is important to note that this benchmark value is for a very different electrochemical system than the one under study in the present work. Calculations based on more complex double layer theory compatible with solvent free ionic liquids has given capacitance estimates of approximately 6 μF cm^{-2} at a metallic interface at 0 V [41,42]. Experimentally, both low temperature CVD carbon [43] and solvent free ionic liquids [44] result in reduced C_{sp}, with values in these systems generally 1 – 3 μF cm^{-2}. It is not clear why the C_{sp} value is anomalously low for the 18 μm

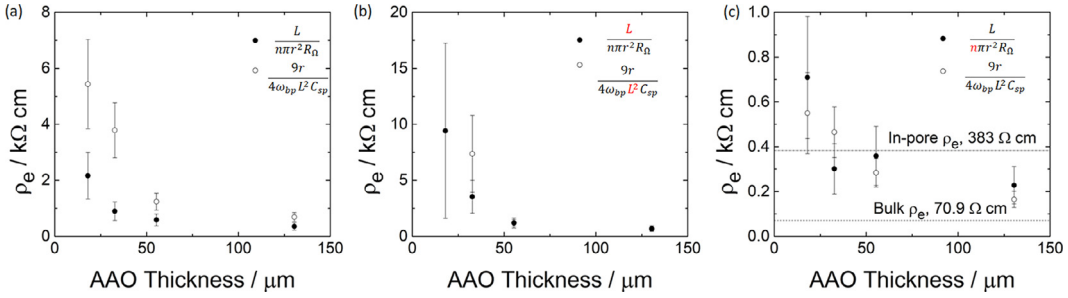

Fig. 7. Calculated values of electrolyte resistivity within the electrode pores based on Eq. (5) (filled circles) and Eq. (8) (open circles). The uncorrected resistivity (a) shows a strong dependence on template thickness which is unexpected. The reduced electrochemically active area can be accounted for either by (b) reducing L or (c) by reducing n. The L reduction still leads to an unwanted dependence on AAO thickness. Reducing n, the number of pores, leads to the most consistent value, an average of 383 Ω cm. This is more than five times higher than the reported bulk value of 70.9 Ω cm. No matter how the reduced area is accounted for, the resistivity in the pores was calculated to be much higher than in the bulk.

electrode, however, the resistivity results in Fig. 7 indicate that the Brug capacitance does give a meaningful value. The measurement model was unable to match the capacitance determined by the Brug formula for these samples, indicating that it may not be reliable for determining the capacitance of porous electrodes. Some authors have proposed that the measured capacitance of nanostructured electrodes may be described as a quantum capacitance in series with the double-layer capacitance [45]. The VACNT walls are believed to be sufficiently thick (~9.5 nm) to allow for comparison to the evaporated carbon control sample. The de Levie model formulas cannot distinguish between the individual contributions of the quantum or double layer capacitances; thus, the specific capacitance reported in the present work is an effective capacitance that may account for both the double-layer and quantum capacitances.

The values of electrolyte resistivity are shown in Fig. 7, calculated from Equations 5 (filled circles) and 8 (open circles) for each AAO thickness. In Fig. 7a, the resistivity was calculated based on the expected pore dimensions and the parameters obtained from the EIS fitting, using the specific capacitance normalized to the electrochemically active area only. The resistivity is seen to increase drastically as template thickness decreases, and there are inconsistencies between Eqs. (5) and (8) for the same samples. Since the electrochemically active area is different from the expected area, the effective pore dimensions should be adjusted to account for the reduced active area. Since the anodization voltage and CVD parameters were constant for all samples, the pore radius was assumed to be unchanged. The reduction in active area could be the result of incomplete wetting of the electrode by the ionic liquid, in which case the effective pore length should be reduced, shown in Fig. 7b. The L-adjusted resistivity again shows a strong dependence on template thickness, and the error in the thinner samples makes drawing conclusions about the resistivity difficult. A constant error in the AAO thickness of 1.4 μm was used based on measurements of other samples. Reducing the template length causes the error as calculated by Monte Carlo simulations to be unacceptably high. Based on the TEM images in Fig. 6, there is evidence that some pores are being blocked during the CVD process. Adjusting for n as in Fig. 7c gives the most consistent resistivity value across all samples, with an average in-pore resistivity of 383 Ω cm. This is more than five times higher than the reported bulk resistivity of 70.9 Ω cm [46,47]. In all cases, there is good agreement in the values obtained from the two equations used. Eq. (5) is based only on the dimensions of the sample determined from SEM, while Eq. (8) also requires C_{sp} which was calculated from the Brug formula. The agreement between the methods indicates that the value of C_{sp} is meaningful, even the anomalously low value calculated for the thinnest sample. Davenport et al. reported that for pores larger than 20 nm in diameter, bulk resistivity was recovered for solvent free ionic liquids [11]. Here it is shown than even with nanopores of average diameter 24.4 nm, resistivity is several times greater than in bulk for neat EMIM-BF4, no matter how the reduced area is accounted for. This finding emphasizes the importance of rational design of EDLC pore structure, since even pores well within the mesopore regime can have detrimental effects on the power performance of supercapacitors [4,48].

In the de Levie model, there are two major simplifying assumptions whose impact on the calculated resistance should be considered. First, the electrode is assumed to be ideally polarizable, i.e. its resistance is 0. The de Levie model can be modified to account for both electrode and electrolyte resistivity [18], but these more complex equations have not been able to fit all data sets. In addition, the resistances of the electrode and electrolyte are coupled in the fitting parameters, making it impossible to find the value of one without knowing the value of the other from a separate measurement. The second major assumption is that the resistance of the electrolyte within the pore, ρ_e, is constant. Hirschorn et al. [49] and Orazem et al. [50] have previously used power law distributions of resistivity through films to accurately determine oxide film thickness from EIS data. If ρ_e is not constant and instead changes along the length of the pore, then the value obtained by the de Levie model may only be the average value of the resistivity within the pore. However, agreement in ρ_e obtained from both long and short pores in Fig. 7c indicates that the resistivity is indeed constant as assumed.

There are several physical phenomena which have previously been reported which may help to explain the increased resistivity. Comtet et al. used tuning fork AFM measurements to determine that solvent free ionic liquids develop solid-like properties when confined to critical dimensions between conducting surfaces due to image force-induced capillary freezing [51]. For a sample of highly ordered pyrolytic graphite, the critical distance for solid-like formation was ~50 nm, and this distance increased with increasing conductivity of the confining surfaces. The critical distance for capillary freezing is greater than the diameter of the carbon pores in the present work, meaning that the ionic liquid may be much stiffer than expected within the pores and therefore exhibit decreased ionic conductivity. Iacob et al. performed measurements of ionic liquid diffusivity within SiO_2 nanopores ~6.5 nm in diameter by broadband dielectric spectroscopy [12]. The authors found that the diffusivity for the as-made, hydrophilic pores was ~10x lower than the bulk value, but by modifying the SiO_2 surface character to hydrophobic, the diffusivity nearly recovered its bulk value. The surface of low temperature grown carbon is known to be functionalized with hydrophilic oxygen containing groups [52–55]. It is possible, then, that this surface functionality plays a major role in the resistivity of ionic liquids even in relatively large pores of ~25 nm in diameter.

5. Conclusion

Several ordered porous VACNT electrodes were analyzed using electron microscopy and EIS. By fitting the EIS data using the de Levie model, CPE parameters Q and α were obtained. By comparing the value of Q for porous samples to that of a non-porous control, the electrochemically active surface area of the VACNT electrodes was determined to be much lower than expected based on the observed pore dimensions. TEM images of individual CNTs indicated that the reduced electrochemically active area may be due to blockages in CNTs formed during the CVD process. Thinner templates showed lower ratios of active-to-expected area, indicating that they are more prone to CVD blockages. The ordered structure of the AAO allowed for detailed analysis of the EIS spectra, and values of the electrolyte resistivity within the pores was determined to be at least five times greater than the bulk resistivity of 64–71 Ω cm. Such drastic increases in resistivity had previously been reported only for pores below 20 nm in diameter, while here they are shown in pores approximately 25 nm in diameter. The increase in resistivity was attributed to layering of the ionic structure at the electrode interface. Such layering inevitably leads to radial concentration gradients within pores which are not accounted for in the de Levie model. The effect of these radial concentration gradients on the equations governing the current distribution within a pore might be the focus of a future study. As supercapacitors are designed with smaller pores, there is a tradeoff between power delivery and energy density. Knowledge of the behavior of electrolytes in nanopores can spur rational design of high performing devices.

Credit Author Statement

Conceptualization: Gibson P. Scisco, Mark E. Orazem, Kevin S. Jones, Kirk J. Ziegler

Data Curation: Gibson P. Scisco

Formal analysis: Gibson P. Scisco

Funding acquisition: Kevin S. Jones, Kirk J. Ziegler

Investigation: Gibson P. Scisco

Methodology: Gibson P. Scisco, Mark E. Orazem, Kevin S. Jones, Kirk J. Ziegler

Project administration: Kevin S. Jones, Kirk J. Ziegler

Resources: Kevin S. Jones, Kirk J. Ziegler

Software: Mark E. Orazem, Kevin S. Jones, Kirk J. Ziegler

Supervision: Mark E. Orazem, Kevin S. Jones, Kirk J. Ziegler

Validation: Gibson P. Scisco, Mark E. Orazem, Kevin S. Jones, Kirk J. Ziegler

Visualization: Gibson P. Scisco, Mark E. Orazem, Kevin S. Jones, Kirk J. Ziegler

Writing – original draft: Gibson P. Scisco

Writing – review and editing: Gibson P. Scisco, Mark E. Orazem, Kevin S. Jones, Kirk J. Ziegler

Declaration of Competing Interest

The authors declare that they have no known competing financial interests or personal relationships that could have appeared to influence the work reported in this paper.

Acknowledgments

The authors would like to thank Mainstream Engineering Corporation for their useful discussions related to this project. This material is based upon work supported by the United States Air Force under Contract No. FA9302-17-C-0001. Any opinions, findings and conclusions or recommendations expressed in this material are those of the author(s) and do not necessarily reflect the views of the United States Air Force. DISTRIBUTION STATEMENT A. Approved for public release; Distribution is unlimited 412TW-PA-21115.

References

[1] M. Salanne, B. Rotenberg, K. Naoi, K. Kaneko, P.L. Taberna, C.P. Grey, B. Dunn, P. Simon, Efficient storage mechanisms for building better supercapacitors, Nat. Energy (2016), doi:10.1038/nenergy.2016.70.

[2] S. Roldán, Z. González, C. Blanco, M. Granda, R. Menéndez, R. Santamaría, Redox-active electrolyte for carbon nanotube-based electric double layer capacitors, Electrochim. Acta 56 (2011) 3401–3405, doi:10.1016/j.electacta.2010.10.017.

[3] G. Li, J. Li, T. Li, K. Wang, TiO_2 nanotube arrays on silicon substrate for on-chip supercapacitors, J. Power Sources 425 (2019) 39–43, doi:10.1016/j.jpowsour.2019.03.120.

[4] J. Chmiola, G. Yushin, Y. Gogotsi, P. Simon, P. Taberna, Anomalous increase in carbon capacitance at pore sizes less than 1 nm, Science 313 (2006) 1760–1763, doi:10.1126/science.1127826.

[5] J.M. Griffin, A.C. Forse, W.Y. Tsai, P.L. Taberna, P. Simon, C.P. Grey, *In situ* NMR and electrochemical quartz crystal microbalance techniques reveal the structure of the electrical double layer in supercapacitors, Nat. Mater. (2015), doi:10.1038/nmat4318.

[6] M.P.S. Mousavi, B.E. Wilson, S. Kashefolgheta, E.L. Anderson, S. He, P. Bühlmann, A. Stein, Ionic liquids as electrolytes for electrochemical double-layer capacitors: structures that optimize specific energy, ACS Appl. Mater. Interfaces (2016), doi:10.1021/acsami.5b11353.

[7] D.W. Chung, M. Ebner, D.R. Ely, V. Wood, R.Edwin García, Validity of the Bruggeman relation for porous electrodes, Model. Simul. Mater. Sci. Eng. 21 (2013), doi:10.1088/0965-0393/21/7/074009.

[8] G. Madabattula, S. Kumar, Model and measurement based insights into double layer capacitors : voltage-dependent capacitance and low ionic conductivity in pores, J. Electrochem. Soc. 167 (2020) 080535, doi:10.1149/1945-7111/ab90aa.

[9] K. Wang, Y. Wang, Y. Wang, E. Hosono, H. Zhou, Mesoporous carbon nanofibers for supercapacitor application, J. Phys. Chem. C 113 (2009) 1093–1097, doi:10.1021/jp807463u.

[10] W.M. Deen, Hindered transport of large molecules in liquid-filled pores, AIChE J. 33 (1987) 1409–1425, doi:10.1002/aic.690330902.

[11] M. Davenport, A. Rodriguez, K.J. Shea, Z.S. Siwy, Squeezing ionic liquids through nanopores, Nano Lett. 9 (2009) 2125–2128, doi:10.1021/nl900630z.

[12] C. Iacob, J.R. Sangoro, P. Papadopoulos, T. Schubert, S. Naumov, R. Valiullin, J. Kärger, F. Kremer, Charge transport and diffusion of ionic liquids in nanoporous silica membranes, Phys. Chem. Chem. Phys. 12 (2010) 13798–13803, doi:10.1039/c004546b.

[13] G.P. Scisco, K. Haynes, K.S. Jones, K.J. Ziegler, Single step bonding of thick anodized aluminum oxide templates to silicon wafers for enhanced system-on-a-chip performance, J. Power Sources 474 (2020) 228643, doi:10.1016/j.jpowsour.2020.228643.

[14] C. Guerra, M. Sancy, M. Walczak, D. Silva, C. Martínez, B. Tribollet, C. Aguilar, Evolution of oxide film on the internal porosity of Ti-30Nb-13Ta-2Mn alloy foam, Electrochim. Acta 283 (2018) 676–682, doi:10.1016/j.electacta.2018.05.010.

[15] O.E. Barcia, E. D'Elia, I. Frateur, O.R. Mattos, N. Pébère, B. Tribollet, Application of the impedance model of de Levie for the characterization of porous electrodes, Electrochim. Acta 47 (2002) 2109–2116, doi:10.1016/S0013-4686(02)00081-6.

[16] R. de Levie, On porous electrodes in electrolyte solutions—IV, Electrochim. Acta 9 (1964) 1231–1245, doi:10.1016/0013-4686(64)85015-5.

[17] M. Obermaier, A.S. Bandarenka, C. Lohri-Tymozhynsky, A comprehensive physical impedance model of polymer electrolyte fuel cell cathodes in oxygen-free atmosphere, Sci. Rep. 8 (2018) 1–9, doi:10.1038/s41598-018-23071-5.

[18] J. Bisquert, Influence of the boundaries in the impedance of porous film electrodes, Phys. Chem. Chem. Phys. 2 (2000) 4185–4192.

[19] R. Jurczakowski, C. Hitz, A. Lasia, Impedance of porous Au based electrodes, J. Electroanal. Chem. 572 (2004) 355–366, doi:10.1016/j.jelechem.2004.01.008.

[20] F. Hilario, V. Roche, A. Moreira, J. Junior, R. Pereira, Application of the transmission line model for porous electrodes to analyse the impedance response of TiO_2 nanotubes in physiological environment, Electrochim. Acta 253 (2017) 599–608, doi:10.1016/j.electacta.2017.09.045.

[21] C. Merlet, C. Péan, B. Rotenberg, P.A. Madden, B. Daffos, P.L. Taberna, P. Simon, M. Salanne, Highly confined ions store charge more efficiently in supercapacitors, Nat. Commun. (2013), doi:10.1038/ncomms3701.

[22] Z. Li, G. Jeanmairet, T. Méndez-Morales, M. Burbano, M. Haefele, M. Salanne, Confinement effects on an electron transfer reaction in nanoporous carbon electrodes, J. Phys. Chem. Lett. (2017), doi:10.1021/acs.jpclett.7b00458.

[23] R. Futamura, T. Iiyama, Y. Takasaki, Y. Gogotsi, M.J. Biggs, M. Salanne, J. Ségalini, P. Simon, K. Kaneko, Partial breaking of the Coulombic ordering of ionic liquids confined in carbon nanopores, Nat. Mater. (2017), doi:10.1038/nmat4974.

[24] A. Lasia, Electrochemical Impedance Spectroscopy and its Applications, Springer, New York, NY, 2014, doi:10.1007/978-1-4614-8933-7.

[25] G.J. Brug, A.L.G. van den Eeden, M. Sluyters-Rehbach, J.H. Sluyters, The analysis of electrode impedances complicated by the presence of a constant phase element, J. Electroanal. Chem. 176 (1984) 275–295, doi:10.1016/S0022-0728(84)80324-1.

[26] C. Hitz, A. Lasia, Determination of the kinetics of the hydrogen evolution reaction by the galvanostatic step technique, J. Electroanal. Chem. 532 (2002) 133–140, doi:10.1016/S0022-0728(02)00760-X.
[27] L. Birry, A. Lasia, Studies of the hydrogen evolution reaction on Raney nickel-molybdenum electrodes, J. Appl. Electrochem. 34 (2004) 735–749, doi:10.1023/B:JACH.0000031161.26544.6a.
[28] R. Karimi Shervedani, A. Lasia, Evaluation of the surface roughness of microporous Ni-Zn-P electrodes by *in situ* methods, J. Appl. Electrochem. 29 (1999) 979–986, doi:10.1023/A:1003577631897.
[29] J. Ahn, S. Cho, J. Min, Impedance spectroscopy of highly ordered nano-porous electrodes based on Au-AAO (Anodic Aluminum Oxide) structure, Nanosci. Nanotechnol. 13 (2013) 7482–7486.
[30] W. Watson, M.E. Orazem, EIS: measurement model program, ECSarXiv (2020), doi:10.1149/osf.io/kze9x.
[31] H. Liao, W. Watson, A. Dizon, V. Vivier, B. Tribollet, M.E. Orazem, Physical properties obtained from measurement model analysis of impedance measurements, Electrochim. Acta (2020) 1–26, doi:10.1016/j.electacta.2020.136747.
[32] C.L. Alexander, B. Tribollet, M.E. Orazem, Contribution of surface distributions to constant-phase-element (CPE) behavior: 1. influence of roughness, Electrochim. Acta 173 (2015) 416–424, doi:10.1016/j.electacta.2015.05.010.
[33] H. Song, H. Hwang, K. Lee, L.H. Dao, The effect of pore size distribution on the frequency dispersion of porous electrodes, Electrochim. Acta 45 (2000) 2241–2257.
[34] H. Song, Y. Jung, K. Lee, L.H. Dao, Electrochemical impedance spectroscopy of porous electrodes : the effect of pore size distribution, Electrochim. Acta 44 (1999) 3513–3519.
[35] T. Sharma, T. Holm, J.A. Diaz-Real, W. Mérida, Experimental verification of pore impedance theory: drilled graphite electrodes with gradually more complex pore size distribution, Electrochim. Acta 317 (2019) 528–541, doi:10.1016/j.electacta.2019.05.119.
[36] C.L. Alexander, B. Tribollet, M.E. Orazem, Contribution of surface distributions to constant-phase-element (CPE) behavior: 2. capacitance, Electrochim. Acta 188 (2016) 566–573, doi:10.1016/j.electacta.2015.11.135.
[37] S.L. Wu, M.E. Orazem, B. Tribollet, V. Vivier, The influence of coupled faradaic and charging currents on impedance spectroscopy, Electrochim. Acta 131 (2014) 3–12, doi:10.1016/j.electacta.2014.01.120.
[38] S.M. Rezaei Niya, M. Hoorfar, On a possible physical origin of the constant phase element, Electrochim. Acta 188 (2016) 98–102, doi:10.1016/j.electacta.2015.11.142.
[39] X. Chen, X. Huang, J. Huang, Z. Huang, W. Xu, J. Liu, Preparation of well-aligned CNT arrays catalyzed with porous anodic aluminum oxide template, Chin. J. Chem. Phys. 19 (2006) 79–83, doi:10.1360/cjcp2006.19(1).79.5.
[40] D.C. Grahame, Differential capacity of mercury in aqueous sodium fluoride solutions. I: effect of concentration at 25, J. Am. Chem. Soc. 76 (1954) 103–173.
[41] M.Z. Bazant, B.D. Storey, A.A. Kornyshev, Double layer in ionic liquids: overscreening versus crowding, Phys. Rev. Lett. 106 (2011) 046102, doi:10.1103/PhysRevLett.106.046102.
[42] A.A. Kornyshev, Double-layer in ionic liquids: paradigm change? J. Phys. Chem. B 111 (2007) 5545–5557, doi:10.1021/jp067857o.
[43] H.J. Ahn, J.I. Sohn, Y.S. Kim, H.S. Shim, W.B. Kim, T.Y. Seong, Electrochemical capacitors fabricated with carbon nanotubes grown within the pores of anodized aluminum oxide templates, Electrochem. Commun. 8 (2006) 513–516, doi:10.1016/j.elecom.2006.01.018.
[44] A. Balducci, R. Dugas, P.L. Taberna, P. Simon, D. Plée, M. Mastragostino, S. Passerini, High temperature carbon-carbon supercapacitor using ionic liquid as electrolyte, J. Power Sources 165 (2007) 922–927, doi:10.1016/j.jpowsour.2006.12.048.
[45] E. Paek, A.J. Pak, G.S. Hwang, Curvature effects on the interfacial capacitance of carbon nanotubes in an ionic liquid, J. Phys. Chem. C (2013), doi:10.1021/jp408085w.
[46] Iolitec, Technical data sheet: 1-ethyl-3-methylimidazolium tetrafluoroborate, 2012.
[47] J. Vila, L.M. Varela, O. Cabeza, Cation and anion sizes influence in the temperature dependence of the electrical conductivity in nine imidazolium based ionic liquids, Electrochim. Acta 52 (2007) 7413–7417, doi:10.1016/j.electacta.2007.06.044.
[48] K. Breitsprecher, C. Holm, S. Kondrat, Charge me slowly, i am in a hurry: optimizing charge-discharge cycles in nanoporous supercapacitors, ACS Nano 12 (2018) 9733–9741, doi:10.1021/acsnano.8b04785.
[49] B. Hirschorn, M.E. Orazem, B. Tribollet, V. Vivier, I. Frateur, M. Musiani, Constant-phase-element behavior caused by resistivity distributions in films, i. theory, J. Electrochem. Soc. 157 (2010) C452–C457, doi:10.1149/1.3499564.
[50] M.E. Orazem, I. Frateur, B. Tribollet, V. Vivier, S. Marcelin, N. Pebere, A.L. Bunge, E.A. White, D.P. Riemer, M. Musiani, Dielectric properties of materials showing constant-phase-element (CPE) impedance response, J. Electrochem. Soc. 160 (2013) 215–225, doi:10.1149/2.033306jes.
[51] J. Comtet, A. Niguès, V. Kaiser, B. Coasne, L. Bocquet, A. Siria, Nanoscale capillary freezing of ionic liquids confined between metallic interfaces and the role of electronic screening, Nat. Mater. 16 (2017) 634–639, doi:10.1038/nmat4880.
[52] A. Yoshida, I. Tanahashi, A. Nishino, Effect of concentration of surface acidic functional groups on electric double-layer properties of activated carbon fibers, Carbon 28 (1990) 611–615, doi:10.1016/0008-6223(90)90062-4.
[53] S. Kubo, I. Tan, R.J. White, M. Antonietti, M.M. Titirici, Template synthesis of carbonaceous tubular nanostructures with tunable surface properties, Chem. Mater. 22 (2010) 6590–6597, doi:10.1021/cm102556h.
[54] S. Wang, Y. Zhang, N. Abidi, L. Cabrales, Wettability and surface free energy of graphene films, Langmuir 25 (2009) 11078–11081, doi:10.1021/la901402f.
[55] M. Pía Rossi, H. Ye, Y. Gogotsi, S. Babu, P. Ndungu, J.C. Bradley, Environmental scanning electron microscopy study of water in carbon nanopipes, Nano Lett. 4 (2004) 989–993, doi:10.1021/nl049688u.